JOURNAL OF SYNCHROTRON RADIATION

ISSN 1600-5775

Received 13 November 2019
Accepted 3 July 2020

Edited by S. M. Heald, Argonne National Laboratory, USA

‡ These authors have equally directed the project

Keywords: computed tomography; X-ray imaging; image quality; multiscale imaging; pink-beam imaging; biomedical imaging.

Multiscale pink-beam microCT imaging at the ESRF-ID17 biomedical beamline

Alberto Mittone,[a,b] Luca Fardin,[b,c] Francesca Di Lillo,[b,d] Michela Fratini,[e,f] Herwig Requardt,[b] Anthony Mauro,[b] Roberto Arturo Homs-Regojo,[b] Paul-Antoine Douissard,[b] Giacomo E. Barbone,[g] Johannes Stroebel,[g] Mariele Romano,[g] Lorenzo Massimi,[e,h] Ginevra Begani-Provinciali,[e,i] Francesca Palermo,[e,j] Sam Bayat,[k] Alessia Cedola,[e] Paola Coan[g]‡ and Alberto Bravin[b]*‡

[a]CELLS – ALBA Synchrotron Light Source, Carrer de la Llum 2-26, 08290 Cerdanyola del Valles, Barcelona, Spain, [b]European Synchrotron Radiation Facility, 71 Avenue des Martyrs, 38000 Grenoble, France, [c]Hedenstierna Laboratory, Department of Surgical Sciences, Uppsala University, Uppsala, Sweden, [d]Elettra Sincrotrone Trieste SCpA, 34149 Basovizza, Trieste, Italy, [e]CNR-Nanotec (Roma Unit), c/o Department of Physics, La Sapienza University, Piazzale Aldo Moro 5, 00185 Rome, Italy, [f]Santa Lucia Foundation, IRCCS, Via Ardeatina 306, 00179 Roma, Italy, [g]Ludwig Maximilian University, Am Coulombwall 1, D-85748 Munich, Germany, [h]Department of Medical Physics and Biomedical Engineering, University College London, London, United Kingdom, [i]Laboratoire d'Optique Appliquée, ENSTA Paris Tech, 828 Boulevard des Maréchaux, 91120 Palaiseau, France, [j]Department of Physics, University of Calabria, I-87036 Arcavacata di Rende (CS), Italy, and [k]STROBE Laboratory, INSERM UA7, 71 Avenue des Martyrs, 38000 Grenoble, France. *Correspondence e-mail: bravin@esrf.fr

Recent trends in hard X-ray micro-computed tomography (microCT) aim at increasing both spatial and temporal resolutions. These challenges require intense photon beams. Filtered synchrotron radiation beams, also referred to as 'pink beams', which are emitted by wigglers or bending magnets, meet this need, owing to their broad energy range. In this work, the new microCT station installed at the biomedical beamline ID17 of the European Synchrotron is described and an overview of the preliminary results obtained for different biomedical-imaging applications is given. This new instrument expands the capabilities of the beamline towards sub-micrometre voxel size scale and simultaneous multi-resolution imaging. The current setup allows the acquisition of tomographic datasets more than one order of magnitude faster than with a monochromatic beam configuration.

1. Introduction

Synchrotron-based X-ray micro-computed tomography (microCT) is the reference technique to investigate samples at high spatial resolution in three and four dimensions (3D, 4D). Applications cover a broad range of fields, including material science (Maire & Withers, 2014), biomedicine (Zehbe *et al.*, 2010), natural sciences (Moreau *et al.*, 2020), paleontology (Fernandez *et al.*, 2015) and cultural heritage (Bukreeva *et al.*, 2016). Sample sizes span from a few millimetres in diameter up to a dozen centimetres; thus microCT setups are normally installed at beamlines equipped with wigglers, bending magnets or superbend sources; undulators, which deliver beams with a much reduced cross section at the sample position, are instead typically used for submicrometre- and nano-CT imaging applications. The success of microCT at synchrotron radiation facilities relies on the specific properties of the X-ray beams delivered by third-generation sources: (*a*) the possibility of generating beams with a high degree of spatial and temporal coherence allows one to apply phase-contrast imaging techniques; image contrast is originated by phase variations within the sample in addition to the absorption

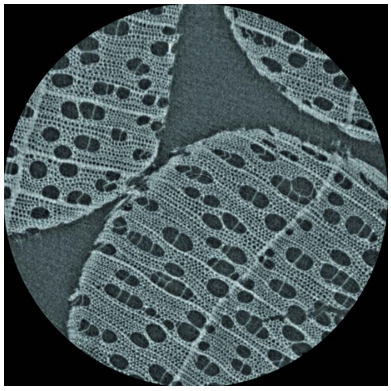

signal (Bravin *et al.*, 2013); (*b*) the laminar geometry of the beam, combined with a suitable detector shape and sample-to-detector distance, opens the possibility of obtaining almost scatter-free images; and (*c*) the high flux over a wide energy spectrum allows monochromatizing the beam whenever necessary (Als-Nielsen & McMorrow, 2011). The use of monochromatic radiation has several advantages in imaging: (i) it allows choosing the most suitable energy for a given sample size and composition, thus optimizing the image contrast and/or minimizing the deposited dose; (ii) it permits avoiding the beam-hardening artifacts often arising in images acquired using polychromatic laboratory sources; and (iii) it allows the application, using optimized parameters, of the dual energy imaging technique using X-ray beam sets of energies bracketing the absorption edge of high-atomic-number elements present in the sample (Thomlinson *et al.*, 2018).

Perfect crystal monochromators typically diffract between 0.2 and ∼1% of the incoming beam, with extremes corresponding to the pure cases of Bragg–Bragg and double bent Laue geometries (Shastri *et al.*, 2002). Thus, depending on the specific characteristics of the source (electron-beam energy, magnetic field, *etc.*), photon fluxes on the samples might become low, with consequent practical limitations in the achievable spatial and temporal resolutions in microCT imaging or in the possibility of performing dynamic studies.

The current imaging research trends are moving towards (i) multi-scale CT, using detection systems with voxel sizes ranging from several tens of micrometres down to the nanoscale, and (ii) time-resolved (4D-CT) studies. Both cases require fluxes that push the limits of the conventional monochromator systems. In the hard X-ray regime, this can be achieved by using multilayer-coated mirrors (MLs) instead of perfect crystals (Smith *et al.*, 1989; Rack *et al.*, 2010). However, because of the grazing geometry used with MLs (glancing angle $<1^{\circ}$), the obtainable beam height is often limited by the multilayer substrate length. As a result, the beam exiting the multilayer is thinner than the beams exiting perfect crystals, thus determining an increased time to scan a vertically extended sample and finally a limited gain in terms of time with respect to using a perfect crystal monochromator.

An alternative method to significantly increase the flux consists of using filtered white-beam radiation, the so-called 'pink-beam' spectrum. The continuous beam spectrum emitted by wigglers and bending magnets is selectively filtered by permanent absorbers inserted in the front-end and along the beamline (typically diamond and/or beryllium windows, and aluminium foils) as well as by removable absorbers. The result is a beam with a broad bandwidth, which can be tuned by varying the magnetic field of the source and/or the type/thickness of the absorbers, with an overall flux that is much higher than that delivered by any monochromator.

Several imaging beamlines around the world have already implemented systems operating in pink-beam mode, including: TOMCAT (Stampanoni *et al.*, 2007), Swiss Light Source, Villigen, Switzerland; ID15 and ID19 (Di Michiel *et al.*, 2005; Weitkamp *et al.*, 2010), European Synchrotron (ESRF), Grenoble, France; L12 and L13, Diamond, Didcot UK; 13-BM-D (Rivers, 2016), the Advanced Photon Source, Argonne, USA; IMBL (Stevenson *et al.*, 2017), Australian Synchrotron, Clayton, Australia; BMIT (Wysokinski *et al.*, 2007), Canadian Light Source, Saskatoon, Canada; and SYRMEP (Tromba *et al.*, 2010), ELETTRA Synchrotron, Trieste, Italy.

Recently, the capabilities of the ID17 biomedical beamline of the ESRF have been extended, providing the possibility to perform microCT with a pink beam at sub-micrometre voxel size. At ID17, when the beamline operates in pink-beam mode, the beam does not intercept any other optical element between the source and the sample except permanent and removable filters and slits. We report here an overview of the main technical details of this imaging system, as well as some preliminary results.

2. Materials and methods

2.1. Source and beamline parameters

Up until its 2020 upgrade to an extremely brilliant source (ESRF-EBS), the ESRF has been operating a third-generation electron storage ring. Intense X-ray beams were produced by 6.04 GeV relativistic electrons passing through the insertion devices located along the 844 m-long storage ring and collected by one of the 44 beamlines in operation. ID17 is one of the long beamlines and is dedicated to biomedical research with a focus on imaging, radiation biology, radiosurgery and radiotherapy. The beamline has two experimental hutches, one inside the ring starting at ∼38.5 m from the W150 wiggler source and one in a satellite building, external to the storage ring building, starting at ∼148.5 m from the source. A detailed description of the beamline instrumentation can be found in the works of Suortti *et al.* (2000), Bravin (2007), Bräuer-Krisch *et al.* (2010), Martínez-Rovira *et al.* (2012) and Crosbie *et al.* (2015). Briefly, in the first hutch, intense-filtered X-ray beams are used mainly for microbeam radiation therapy (MRT) programs (Bräuer-Krisch *et al.*, 2005), while, in the second hutch, only monochromatic radiation is available. The latter hutch is used for experiments of X-ray phase-contrast imaging (analyzer based, propagation based and edge illumination) (Bravin *et al.*, 2013; Coan *et al.*, 2013; Gasilov *et al.*, 2013; Mittone *et al.*, 2018), dual energy imaging techniques (Broche *et al.*, 2017), radiobiology (Ceresa *et al.*, 2018) and radiotherapy (Bräuer-Krisch *et al.*, 2015).

The ID17 beamline sources consist of two wigglers, which can be operated simultaneously. In Table 1, the fundamental parameters are reported together with the machine values influencing the source characteristics. Data reported in this article were acquired before the implementation of the ESRF-EBS upgrade. For the sake of completeness, the parameters of the former storage ring and those of the ESRF-EBS are reported here.

A scheme of the first part of the beamline is shown in Fig. 1. In the first optical hutch (OH1), vacuum sections are separated by two beryllium windows; the main optical instruments are the primary slits, a first set of movable filters, a fast shutter used for MRT irradiation, a double bent Laue Si(111)

Table 1
Machine and wiggler parameters at ID17.

x: horizontal plane; *y*: vertical plane. B_0 is the magnetic field at the minimum allowed gap for the W150 wiggler (24.8 mm). The effective source sizes (Σ_x, Σ_y), expressed as root mean square, have been calculated using *SPECTRA* (Tanaka & Kitamura, 2001). The electron- and the photon-source sizes are reported in terms of σ of a Gaussian distribution. The machine parameters are obtained from the work of Dimper *et al.* (2014).

	Machine parameters	
	ESRF parameters until 2018	ESRF-EBS
σ_x, σ_y (mm)	3.74×10^{-2}, 3.5×10^{-3}	2.72×10^{-2}, 3.4×10^{-3}
ε_x, ε_y (rad mm)	4.0×10^{-6}, 4.2×10^{-9}	1.41×10^{-7}, 4.7×10^{-9}
E (GeV)	6.04	6.00
Source parameters	W150	W125
Λ (mm)	150	125
N periods	11 (10†)	12
B_0 (T)	1.59	1.5
K_{B_0}	22.3	17.5
Σ_x, Σ_y @ 100 mm gap (mm)	7.4×10^{-2}, 2.4×10^{-2}.	6.6×10^{-2}, 2.2×10^{-2}
Σ_x, Σ_y @ 65 mm gap (mm)	1.4×10^{-1}, 2.4×10^{-2}	1.2×10^{-1}, 2.2×10^{-2}.

† The number of effective periods is 10 because the first and last magnets are weak and do not contribute to the effective beam intensity; 10 periods have been considered in the calculations.

monochromator and a personnel safety shutter (PSS). In the first experimental hutch (EH1), two additional beryllium windows, placed in between a long pipe, create an additional vacuum section, which can be dismounted when experiments are carried out in this hutch. An in-air fast shutter, consisting of two rotating tungsten carbide blades, is installed on an optical table and is synchronized with the tomographic acquisition. It prevents extra exposures of the sample during sample imaging pauses, such as the acquisition of reference images, lateral and vertical movements of the samples, and data saving. A kappa-type goniometer (Huber, Germany), used in MRT for sample positioning and irradiation, is placed at ∼42 m from the source. The tomography setup can be installed in the space between the goniometer and the table hosting the detection system, at a position defined according to the experimental parameters used during the experiment. The distance between the source and the sample can vary between 42.6 and 45.5 m from the source.

The magnetic field of the W150 source, described in terms of its harmonic content, is $B(g) = 2.78\exp(-0.02535g) + 0.8425\exp(-0.07538g) - 0.087\exp(-0.081g) - 0.487\exp(-0.16g)$ where g is the wiggler gap; this latter relation is the result of experimental measurements, then fitted by a sum of exponential curves (J. Chavanne, ESRF, personal communication). The opening ranges of the two wigglers are (24.8, 200) mm and (11, 200) mm for the W150 and W125 devices, respectively. Several combinations of beam filters are available as reported in Table 2. In Figs. 2 and 3, spectra of the X-ray beam from the W150 wiggler, calculated using the software *SPECTRA* (Tanaka & Kitamura, 2001), are shown for two gap values (65 mm and 100 mm) and different attenuators (permanent and movable): these correspond to the configurations used for the data acquisitions presented in Section 3.

2.2. Tomography station and detectors

The tomography setup (Fig. 4) consists of a tower of motorized stages used to align the sample and to adjust the setup along six degrees of freedom. All motorized stages are

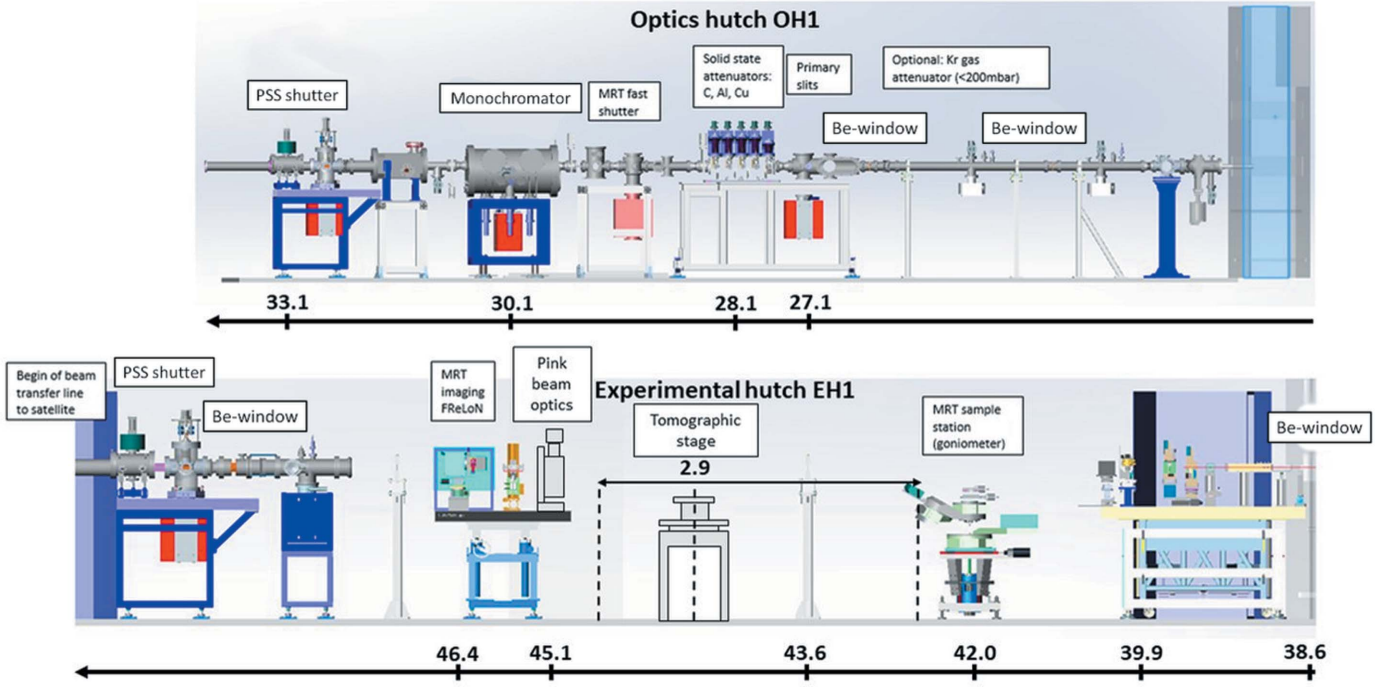

Figure 1
ID17 scheme. At the top, the first optics hutch (OH1); at the bottom, the first experimental hutch (EH1). PSS: personnel safety shutter.

Table 2
Beam attenuators present in the first section of ID17.

Fixed beam attenuators		Movable beam attenuators†	
Material	Thickness (mm)	Material	Thickness (mm)
Be	2.3‡	C	1.15
Al	0.5	Al	0.54/0.71/1.24
		Cu	0.35/0.69/1.04
		Kr (gas attenuator)§	2197

† Different attenuator thicknesses are available. ‡ This represents the total thickness (4 × 0.5 + 0.3 mm). § From the work of Requardt *et al.* (2012), the gas pressure, normally set to 160 mbar, can be adjusted according to the needs.

driven through IcePAPs controllers (Janvier *et al.*, 2013) and remotely piloted through a dedicated *SPEC* (https://certif.com/content/spec/) session. Details of the motors installed on the tomographic tower are reported in Table 3.

The ID17 detection systems include a CCD FReLoN (2048 × 2048 pixels) camera (Coan *et al.*, 2006) and two sCMOS PCO edge 5.5 (2560 × 2160 pixels) cameras (Mittone *et al.*, 2017). All these imaging sensors are coupled with indirect conversion optics (Optique Peter, France). The achievable pixel sizes and corresponding fields of view (FOVs) for the various combinations are reported in Table 4. Concerning the X-ray-to-visible light converters (scintillator screens), several options are available. The choice of the screen is strictly linked to the experimental needs in terms of spatial resolution and detection efficiency. A list of the currently available scintillators is reported in Table 5. To extend the resistance to the radiation damage induced by the intense X-ray beam, a mild N_2 flow is generated in between the scintillator and the optical mirror inside the optics, as described by Zhou *et al.* (2018).

The high-resolution optics used in the pink-beam configuration [Fig. 4(*b*)] allows one to remotely modify the magni-

Table 3
List of motors composing the tomography stage.

LabMotion RT150S	Max speed 200 rev min^{-1}, rotary stage
Faulhaber AM1524-2R-A	± 20 mm range, fine sample alignment
Micos UPM160	150 mm range, lateral sample displacement
Huber 5103.A20-90	90 mm range, fine vertical sample displacement
Huber 5202.10	±15.5° range, angular stage alignment
Phytron + Norcan frame	300 mm range, vertical stage displacement

Table 4
List of selectable magnifications, corresponding numerical apertures (NA) of the optics, FOVs and pixel sizes.

Magnification	NA	Experimental FOV H × V (mm)	Pixel size (µm) (PCO edge 5.5)
1×	– †	16.64 × 2.40 (22.53 × 2.40)	6.5 (11.0‡)
2×	0.055	8.96 × 2.40	3.5
5×	0.140	3.58 × 2.40	1.4
10×	0.280	1.79 × 1.51	0.7

† Data not available. ‡ This value refers to the optics coupled with a FReLoN CCD camera (Coan *et al.*, 2006). The vertical size of 2.4 mm is caused by the limited vertical size of the beam at this station. The sCMOS chip pixel size is 6.5 µm × 6.5 µm while the CCD one is 11 µm × 11 µm.

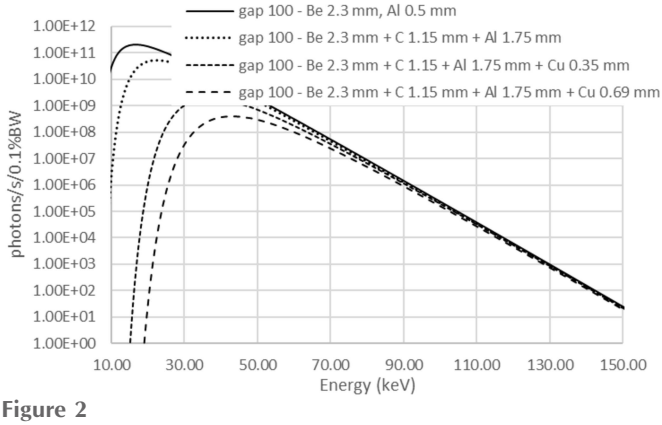

Figure 2
W150 spectra at 100 mm opening gap, including all the permanent filters and selected values of the movable filters (as reported in Table 2). The calculations have been carried out using *SPECTRA* (Tanaka & Kitamura, 2001). The fluxes have been calculated considering a slit opening of 1 mm × 1 mm at 40 m from the source.

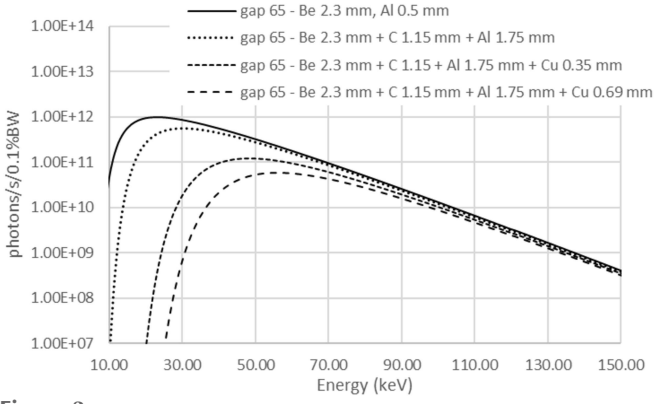

Figure 3
W150 spectra at 65 mm opening gap, including all the permanent filters and selected values of the movable filters (as reported in Table 2). The calculations have been carried out using *SPECTRA* (Tanaka & Kitamura, 2001). The fluxes have been calculated considering a slit opening of 1 mm × 1 mm at 40 m from the source.

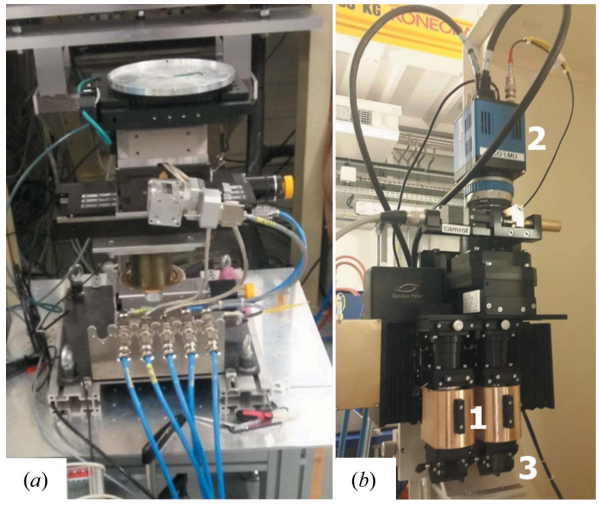

Figure 4
(*a*) CT stage. (*b*) Pink-beam compatible optics (Optique Peter): (1) selectable magnification, (2) PCO edge 5.5 camera and (3) scintillator supports.

Table 5
Available scintillator screens (LuAG, Crytur, Turnov, Czech Republic; GGG, ESRF).

Material	Formula	Thickness (μm)	λ primary peak emission (nm)
GGG:Eu	$Gd_3Ga_5O_{12}$:Eu	19	595
GGG:Eu	$Gd_3Ga_5O_{12}$:Eu	24	595
GGG:Eu	$Gd_3Ga_5O_{12}$:Eu	40	595
LuAG:Ce	$Lu_3Al_5O_{12}$	50	535

fication by choosing the 2×, 5× and/or 10× lenses (Mitutoyo, Japan); however, the optics supports only a combination of two of them at a time. Devoted *SPEC* macros have been developed to remotely change the magnification and to automatically realign the tomography stage with respect to the chosen detection optics (requiring ∼30 s).

The distance between the center of the tomographic stage and the detector could vary in the range 40–290 cm. Following a refurbishment of the instrumentation in EH1, which occurred after the realization of the measurements, the range is now limited to ∼60–100 cm.

2.3. The double detection system for multiscale imaging

Performing 3D imaging at multiple scales is one of the present frontiers of microCT, particularly in biomedicine. For instance, 5–10 μm pixel sizes are sufficient to analyze large-diameter vasculature bone structures, while the visualization of capillaries and of individual cells requires sub-micrometric pixel sizes. For a given detector, the FOV varies with the optics magnification and thus with the effective pixel size. Low magnifications (pixel sizes of 5–10 μm) are useful to visualize the sample architecture and identify regions of interest to be imaged using smaller pixel sizes. The change of optics is time consuming and is prone to errors, particularly when the magnification factors are very different (for instance, a factor of ten). The simultaneous acquisition of low- and high-resolution images, without any change in the optics, represents an interesting solution to overcome these problems. As a drawback, this solution requires image-registration methods to couple the high- and low-resolution images automatically; also, it may lead to a reduction in the FOV of the low-resolution optics because of the limited acceptance window at the level of the first optics.

Following these considerations, the simultaneous acquisition of two tomographic datasets at different spatial resolutions has been implemented at ID17, with a photograph of the corresponding setup reported in Fig. 5. Each of the two optics is coupled with a PCO edge 5.5 detector; alternatively, one with a PCO edge 5.5 for the high-resolution image and one with a FReLoN camera for the low-resolution image. The optics located closer to the sample stage is equipped with a semi-transparent mirror which allows the fraction of X-rays transmitted through the first scintillator to reach the second optics, in turn installed at a distance of ∼1.3 m (in the case of the setup in Fig. 5) with respect to the first optics. The beam transmitted by the mirror passes through a hole drilled in the

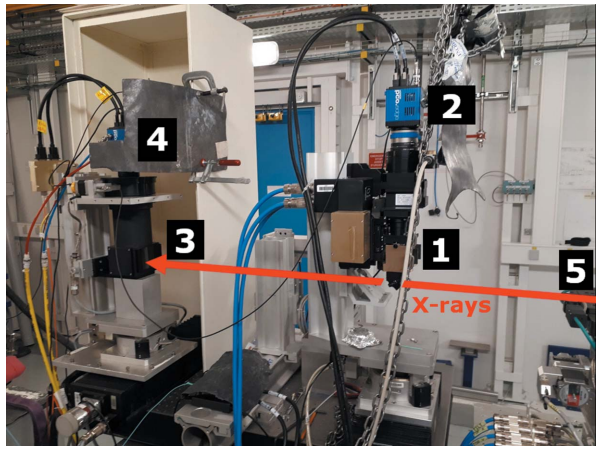

Figure 5
Optical systems for simultaneous low- and high-resolution imaging. (1) High-resolution optics, (2) PCO edge 5.5 camera, (3) low-resolution optics, (4) PCO edge 5.5 camera and (5) CT stage. The X-ray beam is impinging from the right.

aluminium support of the first optics to reach the second scintillator without further light–matter interactions. The distance between the two optics can be varied according to the optimal distance for the second optics (Zabler *et al.*, 2005), which, in turn, depends on the used spectrum and the pixel size of the second optics. The two detectors are connected to two different dedicated servers and simultaneously synchronized with the rotation stage of the tomography station. The synchronization between the rotation stage and the detectors is achieved through a MUSST module (MUSST user manual; ESRF, 2019). The parameters of the acquisition (*i.e.* number of angular projections and integration time) for the two tomography scans can be defined separately for the two detectors. The optics closest to the sample stage is the one providing the smaller pixel size. This design choice is motivated by multiple considerations:

(1) For a given number of quanta on each pixel, the detector with the smaller pixel size requires a higher photon flux.

(2) The smaller the pixel size, the shorter the optimal distance from the sample in free-propagation imaging (Weitkamp *et al.*, 2011).

(3) The beam reaching the second detector is reduced in intensity because of the X-ray absorption by the first scintillator, the combined attenuations by the mirror, the air gap in between the optics and by the effect of the beam divergence.

As previously mentioned, the horizontal beam size accepted by the second optics is currently limited by the first scintillator frame/semi-transparent mirror to 10 mm; however, there are no technical limitations to reshape these elements to fit with the maximum FOV accepted by the second optics. The main source of reduction in spatial resolution is related to the thickness of the scintillator screen.

2.4. CT image acquisition and reconstruction

The two PCO edge 5.5 detectors are connected through the Camera Link Full communication protocol (10 taps, 85 MHz,

850 MB s^{-1} maximum data transfer) connected to the servers via two fiber-optics extenders (Phrontier Technologies, USA); the FReLoN camera is connected through fiber optics only. The two detector servers are equipped with 128 Gb and 64 Gb of RAM, respectively, and are connected to the ESRF computing cluster and storage central server through a 10 Gb network. Because of the high data rate produced by the PCO edge 5.5, the choice of the acquisition parameters (region of interest/number of projections/frame s^{-1}) is linked to the buffer (RAM) available on the server, which limits the performances in the case of high-speed tomography. Tomographic reconstructions are performed on the computing cluster using the *PyHST2* package (Mirone *et al.*, 2014). For a quick image visualization, *ImageJ* (https://imagej.nih.gov/) is available on a dedicated machine equipped with 256 Gb of RAM, while two workstations (128 Gb RAM), equipped with *AMIRA* 6.2 (Thermo Fisher Scientific, France) and *VGStudio MAX* 3.2 (Volume Graphics, Germany), can be used for advanced post-processing operations, for 3D data analysis and rendering.

2.5. Dosimetry

The dose delivered to the sample has been measured in agreement with the protocol reported in the work of Fournier *et al.* (2016). The horizontal gap of the primary tungsten slit was adjusted to obtain a 20 mm-wide X-ray beam at the dosimeter position. A second set of slits in air, positioned on the optical table just upstream of the goniometer, allowed the selection of a 2 mm high beam. The PTW TW31014 (sensitive volume of 0.015 cm^3) ionization chamber (PTW, Freiburg, Germany), connected with a PTW Webline electrometer, was inserted into a 20 cm × 20 cm solid water phantom and positioned at 20 mm depth. The phantom was positioned on the goniometer stage and vertically translated through a 20 mm irradiation field at a constant speed. An in-vacuum fast-shutter device, synchronized with the vertical position of the target, allowed the delivery of the desired dose over the pre-selected target field size (Renier *et al.*, 2002). As proven by Prezado *et al.* (2011), this scanning method is equivalent to a uniform irradiation as long as the beam intensity and the vertical-translation speed remain constant.

The dose integrated while scanning the ionization chamber at a preselected scan speed is equal to

$$D = \frac{\dot{D}\, x\, \mathrm{zbeam}}{v},$$

where D is the measured absorbed dose (Gy), $\dot{D}$ is the dose rate, zbeam is the beam height and v is the scan speed. Measurements were performed at a vertical speed v = 20 mm s^{-1}.

2.6. Pink-beam station commissioning

Multiple experimental measurements have been performed with the aim of evaluating the potential of the pink-beam microCT station for biomedical imaging. Organs imaged in this campaign of experiments were of both animal and human origin; details are reported in the following sub-sections.

2.6.1. Ethical statements. All animals were housed in pathogen-free conditions and treated in agreement with the European guidelines translated into the Italian and French legislations ('Decreto Legislativo 4 marzo 2014, n. 26', and 'Décret n. 2013-118, 01 février 2013', legislative transposition of the Directive 2010/63/EU of the European Parliament and of the Council of 22 September 2010 on the protection of animals used for scientific purposes). All animals were used in the frame of dedicated scientific projects; no animals were specifically sacrificed for the only purpose of collecting data reported in this article. Human samples were provided by the Grenoble University Hospital and were included in a research protocol approved by the reference ethical committee (authorization number AC-2016-2698).

2.6.2. Setup and sample preparation for neuroimaging applications. Images were acquired with final isotropic voxel sizes of 0.7 µm × 0.7 µm × 0.7 µm and 3.5 µm × 3.5 µm × 3.5 µm. The sample-to-detector distances were 1.2 m and 2.1 m for high and low resolution, respectively, which implies a realignment of the setup. The scintillators were a 19 µm-thick GGG:Eu for high resolution and a 40 µm-thick GGG:Eu for low resolution.

The samples were from *ex vivo* mice (wild-type) spinal cords. Before sacrifice, animals were perfused with heparin and physiological solution under deep anesthesia. Spinal cords were then dissected out, fixed in 4% paraformaldehyde for 24 h, and then maintained in 70% alcohol solution until the experiment.

The experimental animal procedures were carried out at the IRCCS AOU San Martino-IST Animal Facility (Genoa, Italy) and at the San Raffaele IRCCS Hospital. Research protocols have been evaluated and approved by the Ethical Committees for animal experimentation of the IRCCS San Raffaele and San Martino (project no. 336). For the high-resolution (low-resolution) mode, having a voxel size of 3.5 µm × 3.5 µm × 3.5 µm (0.7 µm × 0.7 µm × 0.7 µm), a spectrum peaked at 40 keV (47 keV) was used. The scans were performed using the half-acquisition tomographic mode in order to almost double the actual horizontal FOV (Barbone *et al.*, 2018).

2.6.3. Setup and sample preparation for lung-imaging applications. A human lung sample embedded in paraffin was imaged at 0.7 µm × 0.7 µm × 0.7 µm, using the same parameters described in the previous section (Section 2.6.1). The paraffin block, 20 mm × 20 mm × 5 mm in size, was imaged in half-acquisition mode, after selecting a region of interest of 3 mm in diameter and 1.5 mm in thickness. Three thousand equally spaced angular projections were acquired over 360°, with an integration time of 200 ms per projection.

2.6.4. Setup for the double resolution detection system. Two PCO edge 5.5 cameras were used simultaneously and installed on the two independent optics as reported in Fig. 5. The final selected voxel sizes were 0.7 µm × 0.7 µm × 0.7 µm and 11 µm × 11 µm × 11 µm for the upstream and downstream optics, respectively. The sample-to-detector distance for the high resolution was 1.2 m, while it was 2.7 m for the low

resolution, with 1.5 m being the distance between the two optics. The sample-to-detector distances could be further optimized in later trials. A 19 µm-thick GGG:Eu was installed on the high-resolution optics, while a 500 µm-thick LuAG:Ce was mounted on the low-resolution optics. To validate this setup, a bundle of commercial wooded tips has been imaged.

2.6.5. Comparison of pink-beam and double multilayer monochromator images. A comparison of CT images of a phantom acquired with the pink beam and later on with the beam issued by a double multilayer monochromator (DMM) has been performed on a specimen consisting of glass beads, included in a plastic container, with an average diameter of 150 µm. The pink-beam spectrum had a mean energy of ∼40 keV and images were acquired using a PCO edge connected to an optical system providing a 3.5 µm × 3.5 µm × 3.5 µm voxel size. The DMM (20 Å period W/B_4C on 10 cm-long Si substrate), set in diffraction geometry, is installed in the second part of the beamline at ∼137 m from the source. By using the first Bragg diffraction order, it delivers an ∼0.7 mm high beam with a photon density ∼5–10 times higher than that provided by the double bent Laue Si(111) monochromator, installed just downstream of the ML and described in the work of Suortti *et al.* (2000) (the range of values depends on the applied bending). Images were acquired with the DMM set at an energy of 40 keV. The detection system used with the DMM beam is the one described in the work of Mittone *et al.* (2017), combined with an X-ray optics determining a final voxel size of 3.1 µm × 3.1 µm × 3.1 µm. The scintillator used for this experiment was a 250 (50) µm-thick LuAG:Ce for the DMM (pink beam).

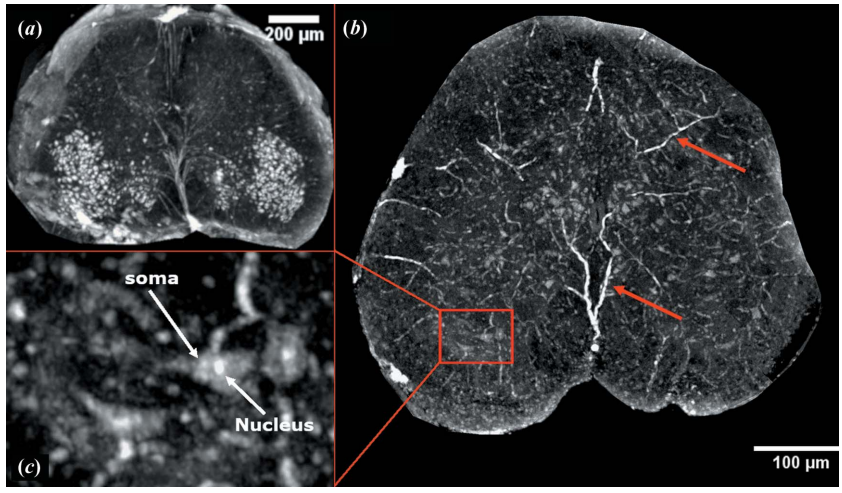

Figure 6
Multiscale CT imaging on a mouse (wild-type) spinal cord (axial view). (*a*) Image acquired using a 3.5 µm × 3.5 µm × 3.5 µm voxel size (reconstruction of 3015 equally spaced angular projections over 360° with an integration time of 80 ms per projection). (*b*) Image acquired at 0.7 µm × 0.7 µm × 0.7 µm voxel size (4001 equally spaced angular projections over 360° with an integration time of 80 ms per projection). (*c*) A magnified region of figure (*b*), where the nucleus and the soma of the single cells are indicated. The images were post-processed using *ImageJ* (https://imagej.nih.gov/); all figures represent the maximum values of a stack of 300 slices. The red arrows in (*b*) point to vessels.

3. Results

3.1. Neuroimaging examples

Fig. 6 reports CT slices of a mouse spinal cord obtained with two different spatial resolutions. The sample was imaged first at a lower resolution [3.5 µm × 3.5 µm × 3.5 µm, see Fig. 6(*a*)] and then the setup was modified for the higher resolution [0.7 µm × 0.7 µm × 0.7 µm, see Figs. 6(*b*) and 6(*c*)]. The data pre-processing, phase retrieval and reconstruction were performed with the *SYRMEP Tomo Project* software (Brun *et al.*, 2017), while the image visualization was created using *ImageJ*. The reported data refer to the lumbar-sacral region of the mouse spinal cord. The images show the maximum values projected of a vertical stack of 300 CT slices. Thanks to this multi-resolution approach, it is possible to simultaneously observe the vascularization and the neuronal network down to the cell nucleus. In particular, it is possible to observe the distribution of the motor neurons (red box) in the ventral horn. Smaller cells, compatible with glia cells around the vessels and motor neurons, can also be distinguished. In addition, the vascular network architecture is also visible. The spatial distribution of the spinal-cord vessels in Fig. 6(*b*) confirms the presence of a small peripheral and large central vascular supply, which is characteristic of the lumbar-sacral region (Cedola *et al.*, 2017).

3.2. Lung-imaging examples

Fig. 7(*a*) presents a CT reconstructed image of a paraffin-embedded human lung tissue. Data were acquired with a voxel size of 0.7 µm × 0.7 µm × 0.7 µm. Fig. 7(*b*) shows a micro-photograph of a hematoxylin/eosin-stained healthy human lung tissue. The comparison between the two images highlights the quasi-histological quality of the CT data. Blood vessels, alveolar walls, aggregates of red blood cells and alveolar macrophages inside the alveolar spaces are clearly visible in the reconstructed CT images.

3.3. Dual resolution detection system

For the double resolution combination, voxel sizes of 6.5 µm × 6.5 µm × 6.5 µm and 0.7 µm × 0.7 µm × 0.7 µm were chosen to obtain simultaneous images permitting the visualization of anatomical features within the overall tissue architecture and then details with a ten times higher resolution. The results are visible in Fig. 8; it is possible to simultaneously visualize the macrostructure of the bundle (*a*) as well as the finer details inside the single wooden tip (*b*).

3.4. Pink-beam versus multilayer monochromator images

The results obtained on glass beads are reported in Figs. 9 and 10, where two regions of 1000 × 1000 pixels are shown.

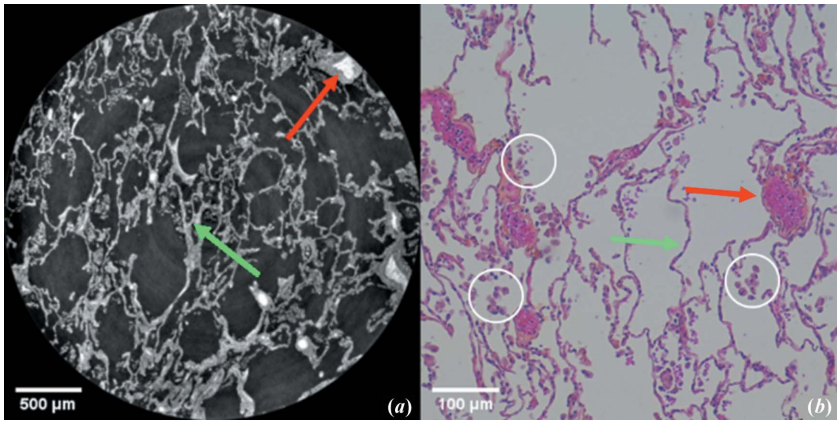

Figure 7
(*a*) A high-resolution CT image of paraffin-embedded human lung tissue with a voxel size 0.7 µm × 0.7 µm × 0.7 µm (3000 equally spaced angular projections over 360° with an integration time of 200 ms per projection). (*b*) Comparison with a microphotograph of a healthy human lung tissue. Blood vessels (red arrows), alveolar walls (green arrows), red blood cells and alveolar macrophages [white circles, in (*b*)] inside the alveolar spaces are visible in the CT, highlighting the histological quality of images produced by this imaging setup.

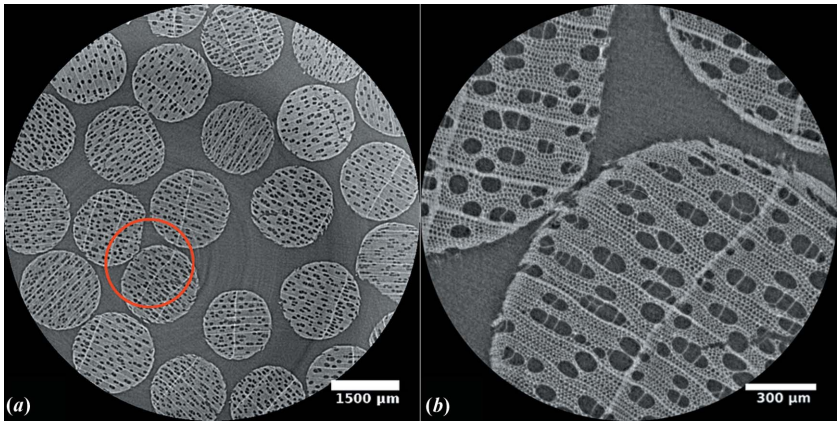

Figure 8
(*a*) Wooden tips bundle with a voxel size of 6.5 µm × 6.5 µm × 6.5 µm. (*b*) Corresponding higher-resolution image with a voxel size of 0.7 µm × 0.7 µm × 0.7 µm. The region covered by (*b*) is highlighted with a red circle in image (*a*). Image (*a*) has been cropped asymmetrically with respect to its center; the red circle represents the center of the original image. The same acquisition parameters have been used for both images: 2500 equally spaced angular projections over 180° with an acquisition time of 100 ms per projection. The propagation distance for the high resolution was 1.2 m and for the low resolution was 2.7 m.

The voxel sizes are 3.5 µm × 3.5 µm × 3.5 µm in the case of pink beam and 3.1 µm × 3.1 µm × 3.1 µm for the DMM-beam case. However, the effective spatial resolution in the case of DMM radiation is poorer than the pink-beam case because of the thicker scintillator (250 µm LuAG:Ce) used for image acquisition. Because of the reduced spatial resolution, the visibility of internal features (holes and inhomogeneities) within the glass beads is highly reduced (Fig. 9). Profiles in Fig. 10 indicate that pink-beam images do not suffer an appreciable loss in image contrast.

3.5. Dosimetry

In order to estimate the dose deposited into the sample during a CT scan using the pink-beam setup, we performed the dosimetry for a range of wiggler gaps (Fig. 11); all measurements were carried out following the protocol reported in Section 2.5. In Fig. 11, the dose rate (expressed in Grays s^{-1}) is plotted as a function of the applied wiggler gap.

4. Discussion

The pink-beam setup, combined with high-resolution optics (Section 2.2), allows for a rapid acquisition of microCT images with voxel sizes down to 0.7 µm × 0.7 µm × 0.7 µm; for instance, it is possible to perform microCT imaging of 3.5 mm × 3.5 mm × 1.5 mm samples within a dozen minutes. Compared with the monochromatic beam delivered by the double bent Laue monochromator (DBLM) (Suortti *et al.*, 2000) and by the DMM system (Section 2.6.5), it allows for a gain in terms of photon density estimated of ∼500 and 50 times, respectively. As a complementary remark, the maximum vertical height of the beam delivered by the DBLM is ∼7 mm while it is ∼0.7 mm for the DMM system (Section 2.6.5); therefore, the number of photons integrated over the entire beam area is similar for the two systems.

Test images acquired in pink beam and reported in Sections 3.1–3.4 clearly show the high image quality achievable, particularly in terms of image contrast. Also, we have shown that it is possible to perform simultaneous imaging of a sample at two resolutions; this configuration allows one to obtain perfect and rapid matching of structures at multiple scales, which is often highly required in biomedical imaging.

The beamline can operate two independent sources (W150 and W125 wigglers, see Table 1). This allows one to obtain, for the 'pink-beam' setup, beam spectra with two tunable energy peaks, one for each source; however, this option was not exploited during the acquisition of the images shown in this article: only the W150 source was always used.

When using the pink-beam setup, the data-acquisition speed is limited by multiple factors, including (i) the detector acquisition, (ii) the maximum speed of the rotation system and (iii) the local network data-transfer rate, but also by the (iv) radiation damage of the sample and the detection system. The performances of the present detection system (PCO edge: 100 frames s^{-1} in full frame mode) can be improved by using faster detectors (f.i. PCO dimax HS: 2277 frames s^{-1}). The rotation speed (200 rev min^{-1}, see Table 3) is not presently a limiting factor. The data flow from the detector has been supported by a sufficiently fast network connection to the data-storage system.

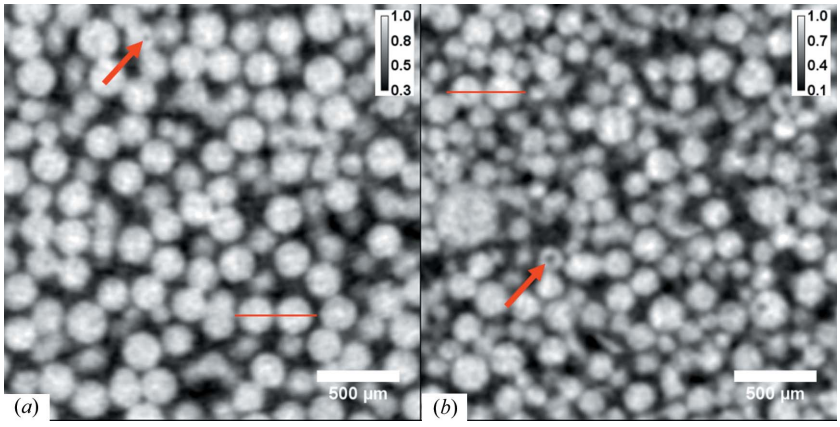

Figure 9
CT images of glass beads (average diameter: 150 µm) included in a plastic container. (*a*) Image obtained using DMM radiation (3.1 µm × 3.1 µm × 3.1 µm voxel size, 2000 angular projections over 180° and a propagation distance of ∼2.2 m with an integration time of 300 ms per projection). (*b*) Pink-beam slice (3.5 µm × 3.5 µm × 3.5 µm voxel size, 2500 angular projections over 180° and a propagation distance of ∼1.8 m with an integration time of 100 ms per projection). The quantitative values have been rescaled to a reference value. The calibration bar reports the values converted into linear attenuation coefficients (cm^{-1}). Two different scale bars are reported to take into account the slightly different voxel sizes. The red arrows indicate internal features within the beads.

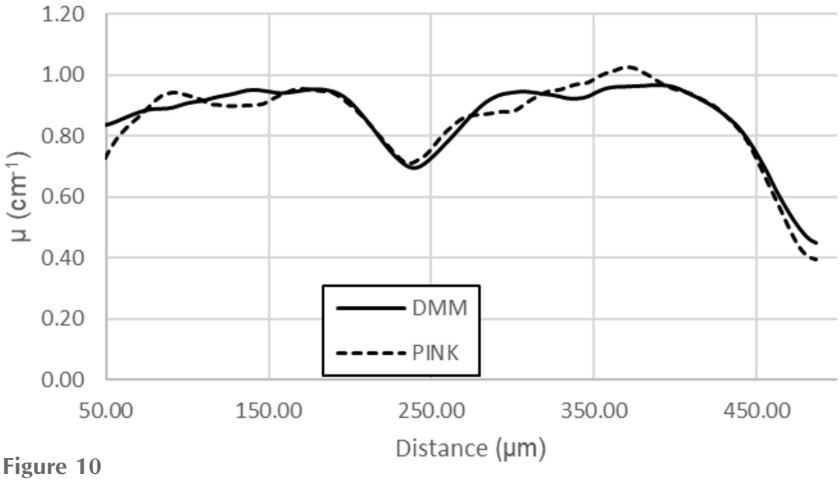

Figure 10
Profiles along the red lines of Fig. 9. The real spatial resolution in the case of the DMM is poorer with respect to the one achieved with the pink beam because of the thickness of the scintillator screen (250 µm for the DMM versus 50 µm in the case of the pink-beam image).

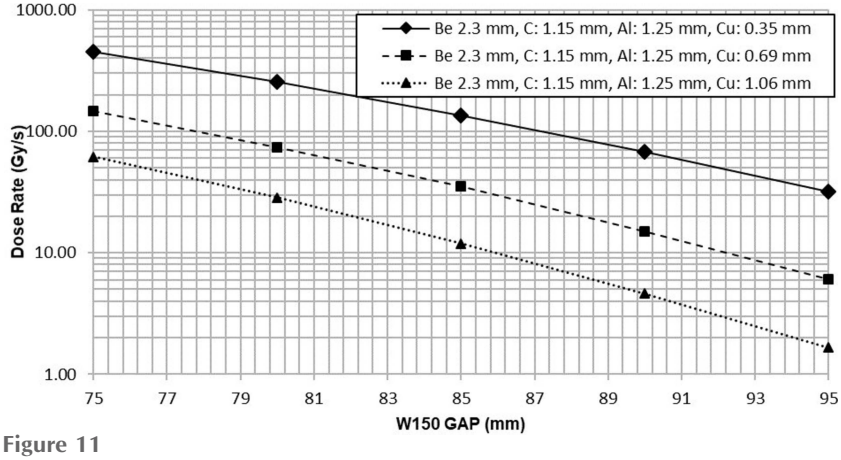

Figure 11
Measured dose rate for different sets of attenuators and gaps of the W150 wiggler.

Radiation damage, determined by high flux rates, is of particular importance in the case of biological samples. Proper sample preparation and fixation protocols are of fundamental importance (paraffin embedding is preferable) to avoid micro- and macro-scopic alterations of the sample structures during the measurements, or of the matrix in which specimens are embedded. For instance, high photon fluxes can cause degassing and create microbubbles in agar–agar during image acquisition, which tend to move along the sample, thus jeopardizing the data. Additionally, high X-ray fluxes can rapidly reduce the performances of the scintillator screen installed in the detection system, with effects that go from screen darkening up to breakdown (Zhou *et al.*, 2018).

X-ray spectra peaked at ∼40 keV, *e.g.* those used in the presented showcases, do not have the inconvenience of determining beam-hardening artifacts in homogeneous samples that have diameters of the order of ∼1 cm (value compatible with the available FOV), as also remarked in the work of Sanchez *et al.* (2012). The largest voxel size available with the current setup is 11 µm × 11 µm × 11 µm. Using larger voxel sizes with the same detection camera would allow to cover the full beam size available in the first experimental hutch, but it would also require larger propagation distances (Weitkamp *et al.*, 2011), which would not fit within the present hutch. In addition, for larger propagation distances, the effect of the finite source size would play an important role in the quality of the results, leading to a loss of contrast and resolution (Arfelli *et al.*, 1998).

5. Conclusions

In this work, we reported an overview of the main characteristics of the new microtomographic station for pink-beam imaging at the ID17 biomedical beamline of the ESRF and its performance in multiscale (sub)microCT imaging. This imaging system, equipped for simultaneous multi-resolution tomography, allows a reduction in the exposure time and therefore in the dose delivered, in multi-scale studies. Future technical improvements may include the use of faster rotary motors and detection systems that enable time-resolved studies.

Acknowledgements

We would like to thank C. Jarnias, T. Martin and B. Restaut from the ESRF for their support. We would also like to thank O. Stephanov from CHUGA for his precious help in the evaluation of the quality of the lung CT images. Authors wish to thank the ESRF for the provision of the beam time (proposals MI1302 and MD1123, and in-house research time).

Funding information

This study was supported by the COST Action CA16122 BIONECA. LF acknowledges the Swedish Research Council (grant no. K2015-99X-22731-01-04 and 2018-02438) and MR acknowledges the German Research Foundation (Deutsche Forschungsgemeinschaft) within the Training Group GRK 2274. PC, JS and GB would like to acknowledge the financial support from the Deutsche Forschungsgemeinschaft (Cluster of Excellence) and the Munich Center for Advanced Photonics (EXE158). MF acknowledges the Italian Ministry of Health under the Young Researcher Grant 2013 (GR-2013-02358177) for their financial support. AC, MF, GBP and FP thanks the European project VOXEL volumetric medical X-ray imaging at extremely low dose (Horizon 2020-Fet Open; Project reference: 665207) and The FISR project 'Tecnopolo di nanotecnologia e fotonica per la medicina di precisione' (funded by MIUR/CNR, CUP B83B17000010001) and the TECNOMED project (funded by Regione Puglia, CUP B84I18000540002).

References

Als-Nielsen, J. & McMorrow, D. (2011). *Elements of Modern X-ray Physics*, 2nd ed. New York: John Wiley & Sons.

Arfelli, F., Assante, M., Bonvicini, V., Bravin, A., Cantatore, G., Castelli, E., Dalla Palma, L., Di Michiel, M., Longo, R., Olivo, A., Pani, S., Pontoni, D., Poropat, P., Prest, M., Rashevsky, A., Tromba, G., Vacchi, A., Vallazza, E. & Zanconati, F. (1998). *Phys. Med. Biol.* **43**, 2845–2852.

Barbone, G. E., Bravin, A., Romanelli, P., Mittone, A., Bucci, D., Gaaβ, T., Le Duc, G., Auweter, S., Reiser, M. F., Kraiger, M. J., Hrabě de Angelis, M., Battaglia, G. & Coan, P. (2018). *Intl J. Radiat. Oncol.* **101**, 965–984.

Bräuer-Krisch, E., Adam, J. F., Alagoz, E., Bartzsch, S., Crosbie, J., DeWagter, C., Dipuglia, A., Donzelli, M., Doran, S., Fournier, P., Kalef-Ezra, J., Kock, A., Lerch, M., McErlean, C., Oelfke, U., Olko, P., Petasecca, M., Povoli, M., Rosenfeld, A., Siegbahn, E. A., Sporea, D. & Stugu, B. (2015). *Phys. Med.* **31**, 568–583.

Bräuer-Krisch, E., Requardt, H., Régnard, P., Corde, S., Siegbahn, E., LeDuc, G., Brochard, T., Blattmann, H., Laissue, J. & Bravin, A. (2005). *Phys. Med. Biol.* **50**, 3103–3111.

Bräuer-Krisch, E., Serduc, R., Siegbahn, E. A., Le Duc, G., Prezado, Y., Bravin, A., Blattmann, H. & Laissue, J. A. (2010). *Mutat. Res. Rev. Mutat. Res.* **704**, 160–166.

Bravin, A. (2007). *Brilliant Light in Life and Material Sciences*, pp. 225–239. Dordrecht: Springer Netherlands.

Bravin, A., Coan, P. & Suortti, P. (2013). *Phys. Med. Biol.* **58**, R1–R35.

Broche, L., Perchiazzi, G., Porra, L., Tannoia, A., Pellegrini, M., Derosa, S., Sindaco, A., Batista Borges, J., Degrugilliers, L., Larsson, A., Hedenstierna, G., Wexler, A. S., Bravin, A., Verbanck, S., Smith, B. J., Bates, J. H. T. & Bayat, S. (2017). *Crit. Care Med.* **45**, 687–694.

Brun, F., Massimi, L., Fratini, M., Dreossi, D., Billé, F., Accardo, A., Pugliese, R. & Cedola, A. (2017). *Adv. Struct. Chem. Imag*, **3**, 4.

Bukreeva, I., Mittone, A., Bravin, A., Festa, G., Alessandrelli, M., Coan, P., Formoso, V., Agostino, R. G., Giocondo, M., Ciuchi, F., Fratini, M., Massimi, L., Lamarra, A., Andreani, C., Bartolino, R., Gigli, G., Ranocchia, G. & Cedola, A. (2016). *Sci. Rep.* **6**, 27227.

Cedola, A., Bravin, A., Bukreeva, I., Fratini, M., Pacureanu, A., Mittone, A., Massimi, L., Cloetens, P., Coan, P., Campi, G., Spanò, R., Brun, F., Grigoryev, V., Petrosino, V., Venturi, C., Mastrogiacomo, M., Kerlero de Rosbo, N. & Uccelli, A. (2017). *Sci. Rep.* **7**, 5890.

Ceresa, C., Nicolini, G., Semperboni, S., Gandin, V., Monfrini, M., Avezza, F., Alberti, P., Bravin, A., Pellei, M., Santini, C. & Cavaletti, G. (2018). *Neurotox. Res.* **34**, 93–108.

Coan, P., Bravin, A. & Tromba, G. (2013). *J. Phys. D Appl. Phys.* **46**, 494007.

Coan, P., Peterzol, A., Fiedler, S., Ponchut, C., Labiche, J. C. & Bravin, A. (2006). *J. Synchrotron Rad.* **13**, 260–270.

Crosbie, J. C., Fournier, P., Bartzsch, S., Donzelli, M., Cornelius, I., Stevenson, A. W., Requardt, H. & Bräuer-Krisch, E. (2015). *J. Synchrotron Rad.* **22**, 1035–1041.

Di Michiel, M., Merino, J. M., Fernandez-Carreiras, D., Buslaps, T., Honkimäki, V., Falus, P., Martins, T. & Svensson, O. (2005). *Rev. Sci. Instrum.* **76**, 043702.

Dimper, R., Reichert, H., Raimondi, P., Ortiz, L. S., Sette, F. & Susini, J. (2014). *ESRF Upgrade Programme Phase II (2015–2022) Technical Design Study*, http://www.esrf.eu/Apache_files/Upgrade/ESRF-orange-book.pdf.

ESRF (2019). *MUSST Multipurpose Unit for Synchronisation, Sequencing and Triggering User Manual*, http://www.esrf.eu/files/live/sites/www/files/Instrumentation/DetectorsAndElectronics/Docs/manuals/musst.pdf (Accessed: 11 June 2019).

Fernandez, V., Buffetaut, E., Suteethorn, V., Rage, J., Tafforeau, P. & Kundrát, M. (2015). *PLoS ONE*, **10**, e0128610.

Fournier, P., Crosbie, J. C., Cornelius, I., Berkvens, P., Donzelli, M., Clavel, A. H., Rosenfeld, A. B., Petasecca, M., Lerch, M. L. F. & Bräuer-Krisch, E. (2016). *Phys. Med. Biol.* **61**, N349–N361.

Gasilov, S., Mittone, A., Brun, E., Bravin, A., Grandl, S. & Coan, P. (2013). *Biomed. Opt. Express*, **4**, 1512.

Janvier, N., Clement, J. M. & Fajardo, P. (2013). *Proceedings of the 14th International Conference on Accelerator and Large Experimental Physics Control Systems (ICALEPCS2013)*, 6–11 October 2013, San Francisco, California, USA, pp. 766–769. TUPPC08

Maire, E. & Withers, P. J. (2014). *Int. Mater. Rev.* **59**, 1–43.

Martínez-Rovira, I., Sempau, J. & Prezado, Y. (2012). *Med. Phys.* **39**, 2829–2838.

Mirone, A., Brun, E., Gouillart, E., Tafforeau, P. & Kieffer, J. (2014). *Nucl. Instrum. Methods Phys. Res. B*, **324**, 41–48.

Mittone, A., Bravin, A. & Coan, P. (2018). *Meas. Sci. Technol.* **29**, 024006.

Mittone, A., Manakov, I., Broche, L., Jarnias, C., Coan, P. & Bravin, A. (2017). *J. Synchrotron Rad.* **24**, 1226–1236.

Moreau, J., Trincal, V., Nel, A., Simon-Coinçon, R., Sallé, V., Le Couls, M., Néraudeau, D. & Fernandez, V. (2020). *Lethaia*, **53**, 106–117.

Prezado, Y., Vautrin, M., Martínez-Rovira, I., Bravin, A., Estève, F., Elleaume, H., Berkvens, P. & Adam, J. F. (2011). *Med. Phys.* **38**, 1709–1717.

Rack, A., Weitkamp, T., Riotte, M., Grigoriev, D., Rack, T., Helfen, L., Baumbach, T., Dietsch, R., Holz, T., Krämer, M., Siewert, F., Meduňa, M., Cloetens, P. & Ziegler, E. (2010). *J. Synchrotron Rad.* **17**, 496–510.

Renier, M., Brochard, T., Nemoz, C. & Thomlinson, W. (2002). *Nucl. Instrum. Methods Phys. Res. A*, **479**, 656–660.

Requardt, H., Renier, M., Brochard, T., Bräuer-Krisch, E., Bravin, A. & Suortti, P. (2012). *J. Phys. Conf. Ser.* **425**, 022002.

Rivers, M. L. (2016). *Proc. SPIE*, **9967**, 99670X.

Sanchez, S., Ahlberg, P. E., Trinajstic, K. M., Mirone, A. & Tafforeau, P. (2012). *Microsc. Microanal.* **18**, 1095–1105.

Shastri, S. D., Fezzaa, K., Mashayekhi, A., Lee, W.-K., Fernandez, P. B. & Lee, P. L. (2002). *J. Synchrotron Rad.* **9**, 317–322.
Smith, A., Riedel, C., Edwards, B., Savage, D., Lai, B., Ray-Chaudhuri, A., Cerrina, F., Lagally, M. G., Underwood, J. & Falco, C. (1989). *Rev. Sci. Instrum.* **60**, 2003–2005.
Stampanoni, M., Groso, A., Isenegger, A., Mikuljan, G., Chen, Q., Meister, D., Lange, M., Betemps, R., Henein, S. & Abela, R. (2007). *AIP Conf. Proc.* **879**, 848–851.
Stevenson, A. W., Crosbie, J. C., Hall, C. J., Häusermann, D., Livingstone, J. & Lye, J. E. (2017). *J. Synchrotron Rad.* **24**, 110–141.
Suortti, P., Fiedler, S., Bravin, A., Brochard, T., Mattenet, M., Renier, M., Spanne, P., Thomlinson, W., Charvet, A. M., Elleaume, H., Schulze-Briese, C. & Thompson, A. C. (2000). *J. Synchrotron Rad.* **7**, 340–347.
Tanaka, T. & Kitamura, H. (2001). *J. Synchrotron Rad.* **8**, 1221–1228.
Thomlinson, W., Elleaume, H., Porra, L. & Suortti, P. (2018). *Phys. Med.* **49**, 58–76.
Tromba, G., Longo, R., Abrami, A., Arfelli, F., Astolfo, A., Bregant, P., Brun, F., Casarin, K., Chenda, V., Dreossi, D., Hola, M., Kaiser, J., Mancini, L., Menk, R. H., Quai, E., Quaia, E., Rigon, L., Rokvic, T., Sodini, N., Sanabor, D., Schultke, E., Tonutti, M., Vascotto, A., Zanconati, F., Cova, M., Castelli, E. & Siu, K. K. W. (2010). *AIP Conf. Proc.* **1266**, 18–23.
Weitkamp, T., Haas, D., Wegrzynek, D. & Rack, A. (2011). *J. Synchrotron Rad.* **18**, 617–629.
Weitkamp, T., Tafforeau, P., Boller, E., Cloetens, P., Valade, J., Bernard, P., Peyrin, F., Ludwig, W., Helfen, L., Baruchel, J., Denecke, M. & Walker, C. T. (2010). *AIP Conf. Proc.* **1221**, 33–38.
Wysokinski, T. W., Chapman, D., Adams, G., Renier, M., Suortti, P. & Thomlinson, W. (2007). *Nucl. Instrum. Methods Phys. Res. A*, **582**, 73–76.
Zabler, S., Cloetens, P., Guigay, J., Baruchel, J. & Schlenker, M. (2005). *Rev. Sci. Instrum.* **76**, 073705.
Zehbe, R., Haibel, A., Riesemeier, H., Gross, U., Kirkpatrick, C. J., Schubert, H. & Brochhausen, C. (2010). *J. R. Soc. Interface.* **7**, 49–59.
Zhou, T., Wang, H., Connolley, T., Scott, S., Baker, N. & Sawhney, K. (2018). *J. Synchrotron Rad.* **25**, 801–807.